Innovative methodology for optimized design and thermo-economic analysis of pillow-plate latent heat thermal energy storage: a case study on heat recovery in the brewing industry

Energy Conversion and Management 341 (2025) 120025

Contents lists available at ScienceDirect

Energy Conversion and Management

journal homepage: www.elsevier.com/locate/enconman

Research Paper

Innovative methodology for optimized design and thermo-economic analysis of pillow-plate latent heat thermal energy storage: a case study on heat recovery in the brewing industry☆

Giorgio Gioanola [a,b], Hector Bastida [a], Elisa Guelpa [b], Vittorio Verda [b], Adriano Sciacovelli [a,c,*]

[a] University of Birmingham, Department of Chemical Engineering, Birmingham, West Midlands, United Kingdom
[b] Polytechnic of Turin, DENERG, Turin, Piemonte, Italy
[c] Technical University of Denmark, Department of Civil and Mechanical Engineering, 2800 Kongens Lyngby, Denmark

ARTICLE INFO

Keywords:
Latent heat thermal energy storage
Pillow plates
Waste heat recovery
Analytical modeling
Brew industry

ABSTRACT

This paper investigates the novel class of pillow-plate latent heat thermal energy storage (PP-LHTES) systems based on the combined use of phase change materials (PCM) of pillow plate heat exchanger technology. Despite recent studies highlighting the promising thermal and economic performance of PP-LHTES systems, their investigation remains limited. In particular, there is a lack of comprehensive thermo-economic analyses to support informed decision-making, especially during the design phase. To address this gap, this paper systematically explores the thermo-fluid and economic performance of PP-LHTES systems by analyzing their design space. An innovative procedure for the optimal design of these devices was developed. The proposed methodology consists of two models: a 1D analytical discretized stationary model, called the design model, and a 1D analytical discretized dynamic model, named the dynamic model. The former is used to determine the design parameters and costs, while the latter is used to validate the designed system under dynamic conditions. The two models are validated against relevant experimental studies taken from the literature and show good performances with errors in the order of 10 % for the design model and 2 % for the dynamic model. A total of 27 configurations were evaluated for potential industrial applications, considering energy storage capacities between 5 and 25 MWh and heat transfer rates ranging from 1 to 5 MW. Representative case studies and operating maps highlight the effects of inlet and outlet temperatures and PCM properties on performance. The layer thickness of the storage material and the channel length depend on discharge time, while the channel count remains constant at a fixed heat transfer rate. The heat exchange area, however, varies with energy storage capacity and heat transfer rate. Additionally, cost maps are systematically examined in terms of energy capacity cost ($/kWh) and power capacity cost ($/kW), highlighting the critical relationship between key PP-LHTES design parameters and the overall cost-competitiveness of the technology. Systems designed for higher temperature differentials (ΔT) demonstrated superior thermal and economic performance, reducing the required heat exchange area and lowering both energy and power capacity costs. An exemplar case study is developed, starting from a reference case in the literature, to illustrate the effectiveness of the proposed methodology. This case study outlines the process of gathering input parameters and demonstrates how the outputs of the two models should be processed to achieve the final design. Ultimately, PP-LHTES emerges as a promising and viable solution for industrial applications at the medium and large scales, with energy capacity costs ranging from 30 to $90 per kWh.

1. Introduction

The IEA [1] set 2050 as the target year to meet net-zero CO2 emissions. While in the field of electricity generation the share of renewables approaches 40 % the decarbonization of the industrial sector remains conspicuously lagging. Indeed, industrial activity contributes to over 15 % of total GHG emissions [2] due to its dependency on natural

☆ This article is part of a special issue entitled: 'ECOS2024_ECM' published in Energy Conversion and Management.

* Corresponding author at: Technical University of Denmark, Department of Civil and Mechanical Engineering, Lyngby, Denmark.
E-mail address: adrsc@dtu.dk (A. Sciacovelli).

https://doi.org/10.1016/j.enconman.2025.120025

Available online 7 June 2025

Nomenclature

Abbreviations and acronyms

CFD	computational fluid dynamics
HEX	heat exchanger
HTF	heat transfer fluid
LHTES	latent heat thermal energy storage
PCM	phase change material
PP	pillow plate

Roman symbols

A	area/surface (m^2)
C	cost ($)
C’	specific cost ($/x)
$_p$	specific heat capacity (J/kg/K)
d	diameter (mm)
E	energy(kWh or MWh)
H	height of the system (m)
IF	installation factor (−)
k	thermal conductivity (W/m/K)
L	length of the system (m)
l	length (m or mm)
$\dot{m}$	mass flow rate (kg/s)
R	thermal resistance (K/W)
Re	Reynolds number (−)
T	temperature (°C)
t	time (h)
U	heat transfer coefficient ($W/m^2/K$)
W	width of the system (c)
w	thickness/distance/width (mm)

Greek symbols

ρ	density (kg/m^3)
N	number(−)
P	power(kW or MW)
Pr	Prandtl number (−)
$\dot{Q}$	heat (W or kW or MW)

Subscript and superscripts

1ch	one channel
1p	one pillow element
c	case
ch	channels
cont	container
disch	discharge
exch	exchange
eval	evaluated
in	inlet
m,log	logarithmic mean
met	metallic
melt	melting
out	outlet
pinch	the pinch point
pl	plates
pp	pillow plates
sp	welding spot
targ	target
tot	total

gas. Evidence demonstrates that the CO2 emissions of the industrial sector are mostly related to the provision of process heat, it is therefore important to act on heat production and dispatch to decarbonize the industrial sector [3]. About 32 % of global heating demand is required in the temperature range from 100 to 500 °C [4]. In such a temperature range process heat is increasingly delivered with high-temperature heat pumps [5], electric boilers [6] and waste heat recovery [7], these technologies showed a huge potential in CO2 reduction and make possible to boost the share of renewables in the industrial sector. The intrinsic intermittency of renewables still represents a problem to fully address the need for reliable and often uninterruptable process heat. Such intermittency necessitates a reconfiguration of operational paradigms, demanding more adaptable modes of operation and greater forms of industrial energy flexibility [8]. Among the key enablers of energy flexibility, thermal energy storage (TES) technology has emerged as a highly attractive solution. Various TES system configurations have been investigated, initially for buildings [9]. More recently, there has been growing interest in their use for industrial [10] and maritime applications [11]. Concerning the computational fluid dynamics (CFD) modeling of thermal energy storage (TES) systems, the enthalpy-porosity method has been applied to simulate the melting process of phase change materials [12]. Furthermore, the feasibility of replacing three-dimensional numerical simulations using the enthalpy-porosity method with two-dimensional simulations has been assessed to reduce computational effort and time [13]. Another study has advanced the numerical modeling of phase change by addressing interface discrepancies, asymmetry in solid–liquid transitions, and equilibrium states [14]. Additionally, a thermal control design has been developed for energy storage systems to manage temperature variations and distribution [15].

Particularly relevant to this study are recent advancements in latent heat thermal energy storage (LHTES) systems. Numerous studies have highlighted the benefits of integrating LHTES into larger thermal systems, not only in reducing the carbon footprint but also in lowering long-term costs [16]. Various LHTES technologies have been investigated through computational modeling [17,18] and experimental studies at multiple scales [19,20]. A less known HEX geometry for LHTES albeit of growing interest and potential, is the so-called pillow-plate heat exchangers (PP-HEX) [21]. A pillow plate (PP) consists of two superimposed metal plates that are initially spot-welded along a specific pattern and then hydroformed to create flow channels for the heat transfer fluid [21]. The PP-HEX, composed of multiple pillow plates connected in parallel, offers high pressure resistance along with favorable thermal properties. Due to these distinctive characteristics, PP-HEXs have been successfully implemented in distillation columns, evaporators, and heat recovery from gas streams Numerical investigations of PPs [22–24], present in the literature, allow a precise and reliable representation of the thermo-fluid performance of such geometry, but the employment of PP-HEX for LHTES remains only marginally explored. Only a limited number of experimental studies has been conducted to systematically investigate the thermo-economic performance of PP-LHTES. Lin et al [25] exclusively investigated a bench-top scale (2–4 kW); however, the work was purely experimental and did not generalize findings to other PP-HEX configurations, scales, or designs. More recently, Galteland et al. [26] reported empirical evidence of the performance of a 200 kWh PP-LHTES operating at an average temperature of approximately 40 °C. In 2025, the installation of LHTES systems with pillow plates on board ships has been investigated with reduced-order modeling and computational fluid dynamics, determining the potential for waste heat recovery [16,19]. Recent advancements in LHTES technology aim to minimize the physical footprint, reduce costs, and optimize the duration of thermal charge and discharge cycles through enhanced heat exchange designs and mechanisms [16,19]. These targets can be achieved through the specific design of the heat exchanger (HE) geometry and the selection of the most suitable phase change material for the conditions of the heat transfer fluid [10]. Research evidence on PP-LHTES thermo-economic potential is currently limited. There is a lack of comprehensive methodology for designing PP-LHTES systems and understanding the effect of key design parameters. This study aims to address these gaps by proposing a thorough thermo-economic methodology for early-stage PP-LHTES design, comprehensively analyzing the impact of design parameters on performance, and estimating technology costs. It provides a novel approach to PP-LHTES analysis, exploring the full design space and offering valuable insights for decision-making. Furthermore, it introduces an innovative methodology for the TES scientific community to deliberate upon the technical and economic facets of PP-LHTES technology.

2. Pillow-Plate latent heat thermal energy storage – system Description and its application context

In Fig. 1 a representation of the integration of PP-LHTES is shown. It is used to mitigate the fluctuation of supply and/or demand of thermal energy from renewable sources and to recover and store waste heat from the industrial process with a back-up connection fed by a fossil fuel (FF) source. The PP-LHTES system is constituted of five main elements the PCM, the HTF, the PP-HEX, the case and the insulation layer. The case hosts the PP-HEX and the PCM.

Two manifolds collect the HTF, one for the inlet and one for the storage outlet. The storage undergoes alternate periods of charge and discharge, while charging the PCM melts and stores heat in latent form, during discharge the heat is released and the PCM solidifies. The insulation layer surrounding the case in Fig. 1 is necessary to prevent heat losses. The main element of the storage is the PP-HEX. It comprises a stack of pillow plates, each made of two spot-welded metal sheets and inflated to realize the internal passages through which the HTF flows. As illustrated in Fig. 2a), PPs are set apart by distance w_{pl}, which constitute a key design parameter to be properly selected to guarantee adequate heat transfer performance. The channels in a PP are designed to make several turns within the same plate, an example is shown in Fig. 2b). The number of channels is equal to the maximum number of welding spots perpendicular to the flow direction (e.g. in Fig. 2b) $N_{ch} = 2$). Each PP is constituted by several PP elements – that is by multiple repetitive elements, one of which is shown in Fig. 2c). Each one of such PP elements is specified by three key dimensions: s_T, $2s_L$ and δ_L.

3. Thermo-economic methodology for exploratory design and assessment PP-LHTES

3.1. Overview of proposed methodology

The methodology aims to an optimized design of PP-TES needed to understand its techno-economic competitiveness. This work starts from the need to study PP technology, to understand how PP-TES can be used for a specific context and application field, the best-suitedsize and the specific costs of this technology. Fig. 3.1 shows the process and highlights in a red box the methodology, it is divided into four main parts, the steady state model, also called the design model. is responsible for the optimal design of the system, given some input and target parameters it is structured to provide, such as output, design and cost maps. The design maps provide the values of the main design parameters in a defined range of power and energy, while the cost maps provide the values of energy capacity cost and power capacity costs. Once the dimensions of the system are chosen, or more sizes are compared to find the best one for the specific case also considering the economic performance, the design parameters are extrapolated from the map and injected into the dynamic model which will provide a deeper analysis of the dynamic behavior of the system. After a deep analysis of the thermal performance of the system, the dimensions are defined and the design process can be considered concluded.

The steady-state model and the dynamic model rely on well-established approaches for the solution of the fluid dynamics and thermodynamics of heat exchangers with submerged plates for thermal energy storage [11,27]. The main correlations applied to model the convective heat transfer between pillow plates and phase change materials rely on consolidated literature references [22–24].

3.2. Design model

3.2.1. Local heat transfer sub-model

As far as the thermo-fluid model is concerned the input parameters are: thermo-physical properties of PCM and HTF, the characteristics of the PP-HEX (including T_{in} and k_{met}), PP element dimensions (including s_T and $2s_L$) and the flow condition (including Re). Additional inputs are the so-called target performance parameters, namely: the target energy storage capacity, discharge time, and target HTF outlet temperature (E^{targ}, t^{targ}_{disch}, T^{targ}_{out}) which should be achieved by selecting adequate geometrical design parameters of the PP-LHTES system. In such regard, the main design outputs of the reduced thermo-fluid model here proposed are w_{pl}, N_{ch}, l_{ch} and A_{exch}. That is the spacing between plates, the number and length of flow channels, and the overall heat transfer area.

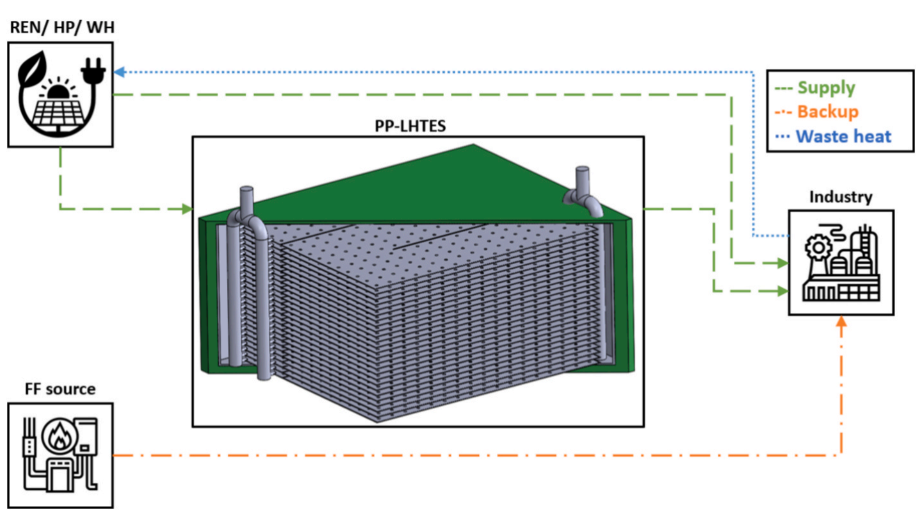

Fig. 1. Integration of the PP-LHTES system with a graphical depiction of its functioning.

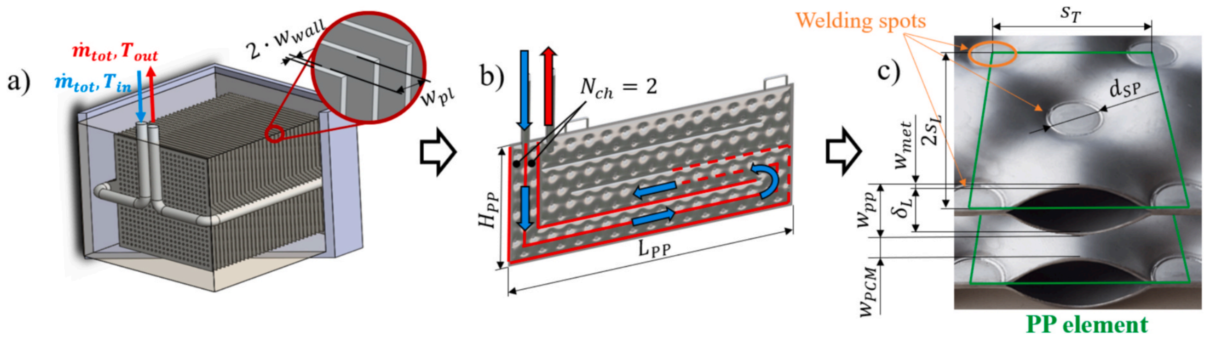

Fig. 2. Three-dimensional design of a PP-LHTES system with highlights of the pillow plate geometry.

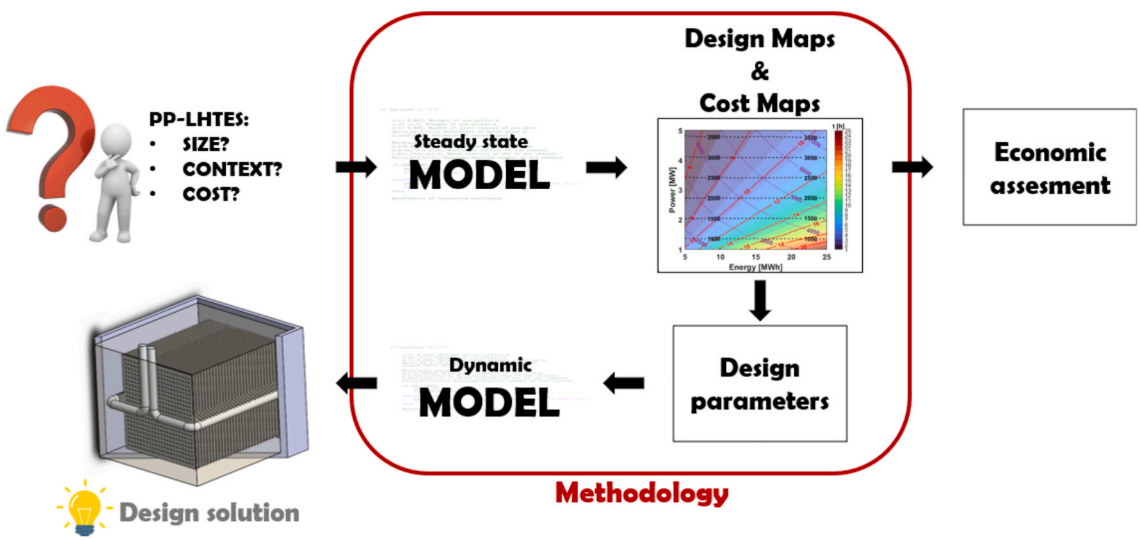

Fig. 3. Schematics of the methodology applied to design the LHTES systems investigated.

To compute the aforementioned design outputs, a *local* heat-transfer analysis was implemented in the reduced thermo-fluid model. Such an approach comprises three main procedures: a) generation of a specialized computational grid, that is a numerical discretization for the PP-HEX geometry; b) associated heat-transfer computation at each cell of the computational grid and c) iterative procedure to identify the design parameters of the PP-LHTES which satisfy the target performance. Fig. 4 illustrates the main concept of what concerns the computational grid and the local heat transfer computation. The cells of the computational grid coincide with the individual PP element (Fig. 4b) constituting the PP-HEX. At each cell of the computational grid heat transfer analysis was performed by applying an equivalent thermal resistances approach, specialized for the analysis of PP-LHTES. It is important to emphasize that evaluation of the thermal resistance was carried out for each discretization element – that is each of PP elements – to account for *local effects* (e.g. changes of temperature difference along the PP-HEX). Thermal resistance was defined as the sum of three contributions (Fig. 4b) and as summarized in Eq. (1). U_{wall} and U_{PCM} are the heat transfer coefficients describing heat conduction through the PP wall and PCM. U_{wall} was computed applying classic heat conduction according to Eq. (2) to the PP wall. Conversely, heat conduction occurring in the PCM layer was described through Eq. (3). Throughout the whole heat analysis, the PCM was assumed to be at a constant temperature coinciding with the nominal melting/solidification PCM temperature. It is important to emphasise that such an assumption is in accordance with the scope of the work, namely to perform early-stage analysis and design of PP-LHTES with the aid of a methodology that allows the rapid exploration of the effect of design parameters and choices. Additionally, as demonstrated by the Validation study discussed in Section 3.4, the proposed methodology predicts the performance of PP-LHTES with a

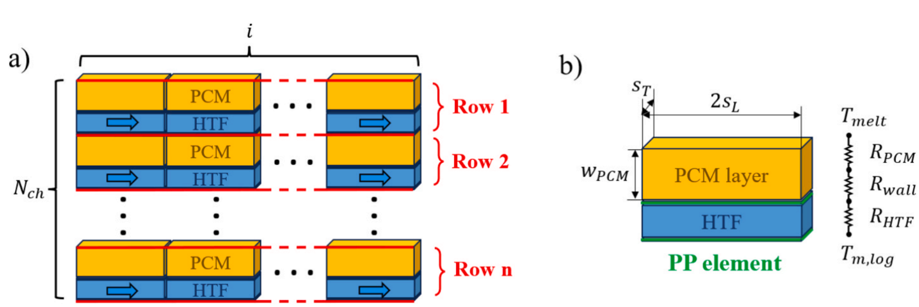

Fig. 4. Discretization of the computational domain of a LHTES heat exchanger.

maximum discrepancy of ~ 13 % with respect of existing experimental data. As far as U_{conv} is concerned, three-dimensional fluid flow patterns due to the complex geometry of PP element affect convective heat transfer occurring on the fluid side of the PP-HEX, as visible in Fig. 2. Various studies, such as [22–24], have been conducted to account for such effects on the convective heat transfer, with most studies concurring on the necessity of using "two-zone" methods to evaluate. The rationale lies in modelling the overall flow pattern by two superimposed simpler flows and associated fluid zones within the PP element, namely the meandering core and the recirculation zone. The hypothesis is that all the flow rates pass through the meandering core which is approximated as a pipe flow while the recirculation zone accounts for stagnation conditions occurring between welded spots of the PP. The same method has been applied in this study for E-type PP elements (E-type are those PP elements in which $2s_L = s_T$). The overall heat transfer coefficient is U_{conv} calculated as in Eq. (8) by following the procedure from Eq. (4) to Eq. (8) with the calculation parameters evaluated as in Table 1.

$$U_{tot} = \frac{1}{R_{tot}A_{1p}} = \left(\frac{1}{U_{PCM}} + \frac{1}{U_{wall}} + \frac{1}{U_{conv}}\right)^{-1} \tag{1}$$

$$U_{wall} = \frac{k_{met}}{w_{met}} \tag{2}$$

$$U_{PCM} = \frac{k_{PCM} \bullet 2}{w_{PCM}} \tag{3}$$

$$\zeta_{z1} = n_6 Re^{n_7} \tag{4}$$

$$Re_{z1} = Re\left(\frac{s^*}{1-\psi_A}\right) \tag{5}$$

$$Nu_{z1} = \frac{\left(\frac{\zeta_{z1}}{8}\right)Re_{z1}Pr}{1.07 + 12.7\sqrt{\left(\frac{\zeta_{z1}}{8}\right)}\left(Pr^{2/3} - 1\right)} \tag{6}$$

$$h = h_{z1}\left(\frac{1-\psi_A}{1-\psi_Q}\right) \tag{7}$$

$$U_{conv} = h \tag{8}$$

Finally, the HTF temperature profile was obtained by coupling the local heat transfer analysis with local energy balance applied to each PP element resulting in Eqs. (9) and (10). It is important to emphasize that such a system of equations is applied to each cell of the computational grid, i.e. to each PP element (Fig. 2c) of the PP-HEX, and under the assumption PCM is at a constant temperature equal to its melting/solidification temperature. Thus, the reduced thermo-fluid model proposed here is strictly applicable during the melting/solidification process occurring within the PP-LHTES system. Nonetheless, as demonstrated through the validation analysis (Section 3.4) the accuracy of the proposed approach attests at about 12 % and thus sufficient for the initial preliminary design analysis of PP-LHTES systems, with the added benefit of enabling rapid and systematic exploration of the effect of design parameters on the target performance.

$$\{\dot{Q}_i = \dot{m}_{1ch} \bullet cp_{HTF} \bullet (T_{i+1} - T_i) \tag{9}$$

$$\dot{Q}_i = \frac{\Delta T_{m,log}}{R_{tot}} \tag{10}$$

Table 1
Parameters for the calculation of the heat exchange coefficient for convection.

n_6	n_7	ψ_A	ψ_Q	s^*	b	c
$2.52c + 0.24$	−0.3	$0.75b + 0.46$	$0.75b + (1.54c - 0.014)$	1	$\frac{d_{sp}}{s_T}$	$\frac{\delta_L}{s_T}$

where $\dot{Q}_i$ is the inlet thermal power, $\dot{m}_{1ch}$ is the mass flow rate of the HTF in the channel, cp_{HTF} is the specific heat at a constant pressure of the HTF, Ti and Ti + 1 are its temperature values at adjacent nodes, $\Delta T_{m,log}$ is its logarithmic mean temperature difference, and R_{tot} is the total thermal resistance.

3.2.2. Iterative procedure

The thermo-fluid dynamic computation illustrated in the previous section was coupled to a bespoke iterative procedure to ensure the PP-LHTES system target performance (E^{targ}, t^{targ}, T^{targ}_{out}) are met by the selection of feasible design parameters. The iterative procedure determines the number of computational cells – which coincides with the total number of PP elements (Fig. 2c) – necessary to meet the outlet temperature constraint (Fig. 5a); subsequently the number of parallel series of PP elements – i.e. the number of "parallel rows" is computed to achieve the desired heat transfer rate P^{targ}.

Finally, results were considered satisfactory if the computed m^{eval}_{PCM} was within ± 5 % of the targeted value as m^{targ}_{PCM}. If m^{targ}_{PCM} exceeds the ± 5 % limit the value of w_{PCM} is increased and the process is repeated until a feasible configuration is obtained. This process is repeated for every combination of E^{targ} and t^{targ}_{disch} as well as for different ΔT and nominal PP-LHTES temperature (i.e. nominal operating temperature). By sweeping the combinations of parameters the whole feasible design space of PP-LHTES system was explored enabling to produce the design and performance maps illustrated in the Results section.

3.3. Economic assessment

The economic assessment was carried out by considering the capital cost of the PP-LHTES as the sum of the HEX cost, the PCM cost and the container cost. The latter is composed of three contributions represented by the casing cost, foundation cost and insulation cost [28]. PCM cost data were collected [29] for three different PCM families organic, salts hydrates and eutectic mixtures. Fig. 6 shows a huge variability for the eutectic compounds cost, while salts hydrate PCMs resulted in the cheapest option with the presence of some outliers. The cost of the HEX is evaluated with the function $C_{HEX} = 702 \bullet IF \bullet A^{0.6907}_{exch}$ valid for plate type heat exchangers [30]. The value of the installation factor (IF) varies in the range 1.5–2 depending on the dimension of the HEX [28]. As said previously the cost of the container is evaluated as the sum of the casing cost $C_c = 2 \bullet \rho_{SS} \bullet L_t \bullet w_c \bullet (H_t + W_t) \bullet C'_{SS}$, cost of foundations $C_f = W_t \bullet L_t \bullet C'_f$ and cost of insulation $C_i = 2 \bullet L_t \bullet (H_t + W_t) \bullet C'_i$.

Where ρ_{SS} is the density of the stainless steel (SS)[kg/m^3], w_c is the thickness of the casing, C'_{SS} is the relative cost of SS equal to 5.1 $/kg [31], C'_f and C'_i are respectively the cost of foundations equal to 1210 $/m^2 and the cost of insulation material equal to 235 $/m^2 [32,32]. L_t, H_t and W_t are respectively total length, height and width of the PP-LHTES. These dimensions were computed considering PPs with a pattern with 4 turns and 10 channels per plate. Finally, the total cost of the PP-LHTES is divided by E and P to obtain the relative energy capacity cost C'_E [$/MWh] and the relative power capacity cost C'_P [$/MW].

3.4. Validation of the design model

In the reference study [33], the authors investigated the behavior of a LHTES system in the heating system, mostly supplied by a heat pump (HP) which increases the water temperature of the hot side from 35 °C to 40 °C with a total power of 26 kW. The storage was designed to store the excess heat during the off-peak hours with an energy requirement of around 200 kWh to reduce the dimension of the HP down to 14 kW. The LHTES was filled with around 3000 kg of CrodaTherm 37 (CT37) [34] and the HTF flowing in the whole system was water. The PP-LHTES was composed of 24 PPs with $w_{pl} = 40mm$. Dimensional limits were imposed for moving the storage in a building with 1.8 m wide corridors and 2 m

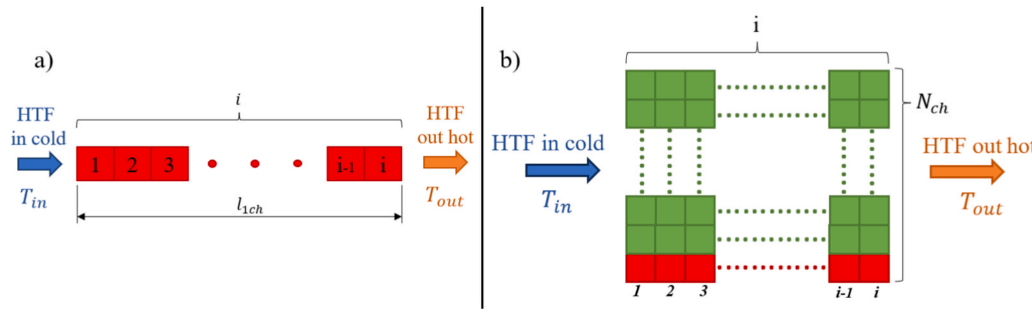

Fig. 5. Graphical representation of the iterative procedure to obtain the design targets: a) outlet temperature, and b) heat transfer rate.

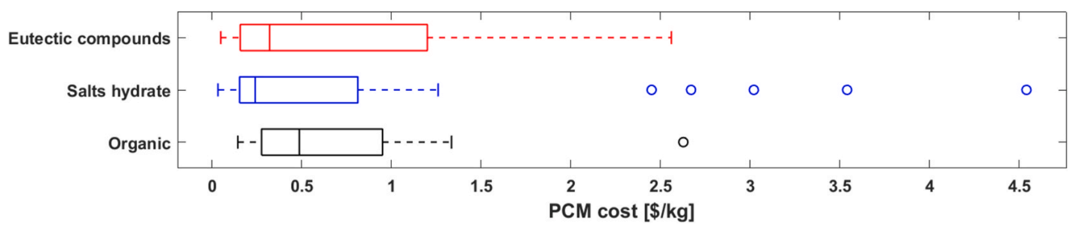

Fig. 6. Estimation of the cost of the PCM materials considered to design the LHTES systems.

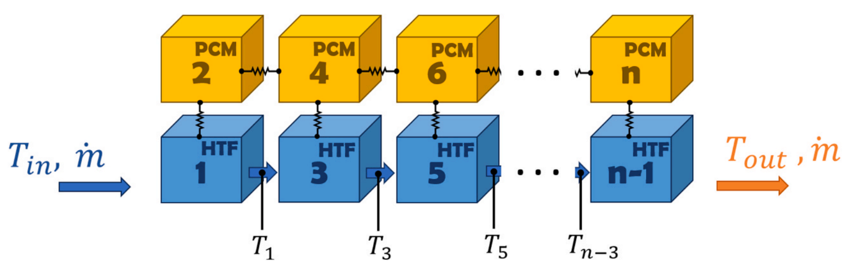

Fig. 7. Discretization pattern for the dynamic model.

high doors. The design model is set up with the following target parameters $E_{tot}^{targ} = 170kWh$, $t^{targ} = 14h$, $T_{in} = 30^{\circ}C$ and $T_{out}^{targ} = 34^{\circ}C$. The properties of the PCM are taken from the reference [33], regarding the HTF the properties of H2O at 34 °C are taken as input. The dimensions set for the PP element are $s_T = 2$, $s_L = 100mm$, $\delta_L = 8mm$, $k_{SS} = 15W/m/K$. The model gave as output the values$l_{1ch} = 6.1$ m and $N_{ch} = 133$ channels, the chosen design for the PPs is a pattern with 2 turns with 5 channels for each plate and a total of 26 plates parallel connected with a pitch of 35 mm. The results are summed up Table 2, they do not vary more than 13.8 % compared to the reference, the value of V_{tot} is the one with the smallest variation, -1% with respect to the reference case [33].

Table 2
Validation of the results of the case analyzed with reference values from [33].

Thermal parameters	Predicted value	Reference value	Percentage variation	Units
E_{tot}	149.3	168	-12.5%	kWh
P_{tot}	12.05	12	*Correctlytargeted*	kW
t_{tot}	12.3	14	-13.8%	h
T_{out}	34.03	34	*Correctlytargeted*	$^{\circ}C$
Geometric parameters				
l_{sys}	2.22	2.25	–	m
h_{sys}	1.67	1.5	*Intherequestedlimit*	m
w_{sys}	1	1.4	*Intherequestedlimit*	m
V_{tot}	0.0371	0.0375	-1%	m^3
N_{pl}	26	24	–	–
A_{tot}	142.7	134.4	$+6.2\%$	m^2
m_{PCM}	2713	3053	-12.5%	kg

3.5. Dynamic model

Once the design parameters of the system. that are $l_{1ch}, A_{exch}, w_{PCM}$ and N_{ch}, are obtained from the design model a first design of the PP-LHTES is deliberated and validated through the dynamic model. Two important inputs are the temperature of the HTF at the inlet (T_{in}) and the value of the mass flow rate $\dot{m}$. Both can be injected into the model as a function of time. Other than the design parameters, the properties of the HTF, PCM and metallic material are given to the dynamic model, regarding the thermal properties they vary with the temperature. The purpose of the dynamic model is to further increase the reliability of the design results of the model and verify the correct behavior of the designed system under conditions of varying mass flow rate and temperature in time. Once the system is dynamically validated and respects the design constraints the first design of PP-LHTES is deliberated. The dynamic model is then used for the estimation of the dynamic performance of the system.

There are three types of inputs given to the dynamic model, the constants or properties, the temperature-dependent properties and the time-dependent inputs. The former are all those characteristics which are steady and do not change in time, they are summed up in Table 3.3.

The second type of inputs are the temperature-dependent inputs. These are all those material properties which change due to a variation in temperature, they are summed up in Table 3.4.

The last type of input is time-dependent. The model is able to take both inlet temperature and inlet mass flow rate as a function of time.

Table 3
Steady input for the dynamic model.

Element	Property	Unit
PP element	s_T	mm
	$2s_L$	mm
	w_{pp}	mm
	δ_i	mm
	d_{hyd}	mm
	V_{PPE}	mm^3
HEX	A_{exch}	m^2
	N_{PPE}	–
	w_{PCM}	mm
	ρ_{met}	kg/m^3
PCM	m_{PCM}	kg
	ρ_{PCM}	kg/m^3

Usually, in this kind of system the mass flow rate as well as the, of course, inlet temperature vary between the charge and discharge phases. Table 4.

Regarding the phase change, it is simulated with the equivalent specific heat (c_p) method. The c_p of the PCM is given to the model as a function of temperature, as in Eq. (11), and it is valid for both the charge and discharge phases.

$$c_p(T) = c_{p,s} + \frac{L}{\Delta T_{SL} \bullet \sqrt{\pi}} \bullet e^{-\frac{(T-T_{melt})^2}{\Delta T_{SL}{}^2}} \tag{11}$$

where c_p is the specific heat [J/(kgK)], $c_{p,s}$ is the specific heat related to sensible heat, T is the current temperature of the PCM, T_{melt} is the melting temperature, L is the latent heat of the PCM and T_{SL} is the solidification and melting temperature of the PCM.

The system is discretized along the direction of the fluid flow. The number of elements is defined a priori depending on the level of accuracy requested for the analysis, the higher the number of elements higher the computational time and the better the accuracy. The number of elements used in the model is 5, as analyzed by Bastida et al. [35] the number of elements does not significantly reduce the error once the number of elements is above 5, with a difference in the absolute temperature error of about 0.1 °C between the case with 100 elements and the case with 5 elements. The system is discretized in PCM and HTF elements so that the temperature of each element can be evaluated as well as the heat exchanged between them. The thermal resistance between PCM and HTF is evaluated in the same way as the design model (Section 3.2), while the thermal resistance between two PCM elements is calculated as a conduction resistance through a wall as in Eq. (12). The outlet temperature from the HTF elements is considered equal to the temperature of the element. while the outlet temperature is evaluated by solving the local thermal problem.

Table 4
Temperature-dependent inputs for the dynamic model.

Element	Property	Unit
PCM	$c_{p,PCM}(T)$	J/kg/K
	$k_{PCM}(T)$	W/m/K
HTF	$c_{p,HTF}(T)$	J/kg/K
	$k_{HTF}(T)$	W/m/K
	$\rho_{HTF}(T)$	kg/m^3
	$\mu_{HTF}(T)$	kg/m/s

$$U_{P-P} = \frac{k_{PCM}(T)}{2s_L} \tag{12}$$

The local thermal problem in the dynamic model is based on a thermal balance for each element or node of the system [22–24]. The balance is imposed by Eq. (13) as the sum of three contributions the inlet term, the outlet term (on the right of the equation) and the storage term (on the left side of the equation).

$$\frac{dE}{dT} = \dot{Q}_{out} - \dot{Q}_{in} \tag{13}$$

where $\dot{Q}_{out}$ and $\dot{Q}_{in}$ [J/s] are the heat flux getting out and in respectively.

When is applied to an HTF element the left side of the equation describes the variation of temperature of HTF in time while, regarding the right side, the inlet power is represented by the mass flow rate of HTF entering the element. The outlet power is divided into two contributions, the power exchanged with the following HTF element, and the power exchanged with the PCM element, this is reported in Eq. (14). When Eq. (13) is applied to a PCM element the left side of the equation describes the variation of temperature of the PCM in time, and the right side is divided into two contributions the energy exchanged with the HTF and the energy exchanged with the following PCM element, as in Eq. (15). In these equations, each property of the materials involved in the heat exchange process has to be considered depending on the temperature of each material at each block.

$$m_1 c_{p,1} \dot{T}_1 = T_{HTFin} c_{p,HTFin} \dot{m}_{HTF} - T_1 c_{p,1} \dot{m}_{HTF} - U_{H-P} A_{H-P} (T_1 - T_2) \tag{14}$$

$$m_2 c_{p,2} \dot{T}_2 = U_{H-P} A_{H-P} (T_1 - T_2) - U_{P-P} A_{P-P} (T_2 - T_4) \tag{15}$$

where m [kg] is the mass, A [m^2] is the heat transfer area ans subscritps 'H' and 'P' stand for HTF and PCM elements, respectively.

These two equations are solved simultaneously to compute the values of $\dot{T}_1$ and $\dot{T}_2$. These two values are then integrated in time to calculate the variation of temperature in time. The local thermal problem is applied to every element of the discretized system to capture the evolution of the temperature of HTF and PCM in time along the length of the system. The discretization process brings to the system of non-linear ODEs which is written in a matrix in Eq. (16).

$$\begin{aligned}\left[\dot{T}_1 \dot{T}_2 \cdots \dot{T}_{i-1} \dot{T}_i \cdots \dot{T}_{N-1} \dot{T}_N\right] = \Bigg[& \frac{T_{HTFin} c_{p,HTFin} \dot{m}_{HTF} - T_1 c_{p,1} \dot{m}_{HTF} - U_{H-P} A_{H-P} (T_1 - T_2)}{m_1 c_{p,1}} \; \frac{U_{H-P} A_{H-P} (T_1 - T_2) - U_{P-P} A_{P-P} (T_2 - T_4)}{m_2 c_{p,2}} \\ & \cdots \frac{T_{i-3} c_{p,i-3} \dot{m}_{HTF} - T_{i-1} c_{p,i-1} \dot{m}_{HTF} - U_{H-P} A_{H-P} (T_{i-1} - T_i)}{m_{i-1} c_{p,i-1}} \; \frac{U_{H-P} A_{H-P} (T_{i-1} - T_i) - U_{P-P} A_{P-P} (T_i - T_{i+2})}{m_i c_{p,i}} \\ & \cdots \frac{T_{N-3} c_{p,N-3} \dot{m}_{HTF} - T_{N-1} c_{p,N-1} \dot{m}_{HTF} - U_{H-P} A_{H-P} (T_{N-1} - T_N)}{m_1 c_{p,N-1}} \; \frac{U_{H-P} A_{H-P} (T_{N-1} - T_N)}{m_N c_{p,N}} \Bigg]\end{aligned} \tag{16}$$

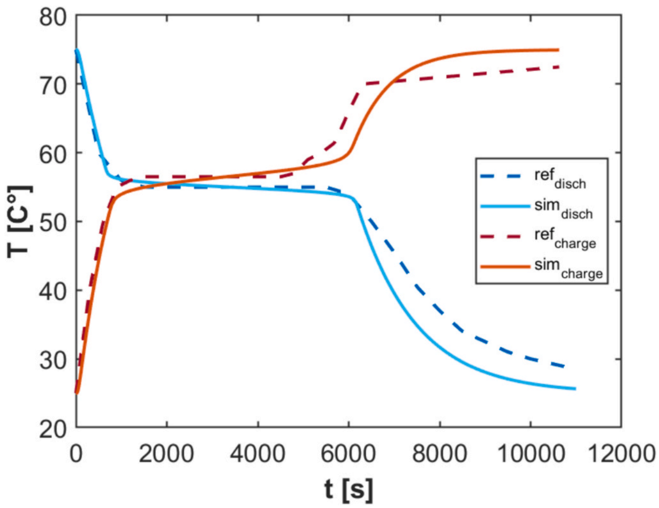

Fig. 8. Comparative plot of the charging and discharging phase simulated with the dynamic model.

3.6. Validation of the dynamic model

Due to the lack of experimental data in the literature, the process of validation for the dynamic model resulted very difficult for an industrial application size, for this reason, the study from Lin et al. [25] has been taken as a reference for the matter of validation.

The validation process consists of the simulation of the PP-LHTES during the charging and discharging phases. The two phases have been analyzed separately since the same was done in the reference study [25]. The plots of the reference curve and the simulated curve, for both the charging and discharging phases, are reported in Fig. 8.

Mean absolute error (MAE) and root mean square error (RMSE) have been calculated for both cases. Regarding the charging phase, the MAE is 1.61 °C while the RMSE is 2.05 °C, while for the discharging phase, the evaluated MAE is 2.06 °C and the RMSE is 2.90 °C. In the case of LHTES systems an important parameter to be analyzed is the duration of the latent phase. Regarding the discharge phase, the model can correctly capture the duration of the latent phase, in fact, the two knees of the simulation curve, one for the beginning of the solidification and the other for the ending, correspond to the ones of the simulated curve, this indicates a good representation of the latent phase. In the case of the charging phase, the first knee, indicating the start of the melting phase, is correctly simulated while in the second knee, indicating the end of the melting phase, a delay of approximately 1000 s (~16 min) can be observed. This discrepancy is due to the natural convection phenomena occurring during the melting phase. The difference in temperature between the melted material and the moving melting front brings to the creation of natural vortices which considerably fasten the melting process. This phenomenon is almost negligible during the solidification process. Moreover, the regime temperature in both simulated charge and discharge is reached faster than the experimental data from the reference, indicating the variability of cp and thermal conductivity of the PCM.

4. Results and Discussion

4.1. Temperature profile and ΔT_{pinch} effect

The temperature of the HTF follows a logarithmic trend of Fig. 9, while TPCM remains constant along the entire length of the storage system due to the assumptions made during the modeling phase. Additionally, comparing the two plots reveals that reducing $\Delta T_{\mathrm{pinch}}$ from 20 °C (Fig. 7a) to 10 °C (Fig. 7b) leads to an approximately 35 % increase in channel length. As the logarithmic mean temperature difference between PCM and HTF decreases, a longer tube is required to achieve a similar heat exchange.

4.2. Exploration of design and thermo-fluid performance and performance comparison

The design maps were built for a heat rate (P) in the range 1–5 MW and for energy content (E) in the range 5–25 MWh, for $Re = 8000$. An example on how to read the map is provided in Fig. 10c) where the design point "Dc" is found starting from E = 15 MWh and P = 3 MW, the values of the parameters are then read from the map: w_{PCM} 25mm, l_{ch} 25m and A_{exch} 9500m^2.

A visual sensitivity analysis can be conducted for all four design parameters. The iso-A_{exch} curves follow a hyperbolic trend showing a similar dependency from both P and E. The curves iso-N_{ch} represented in Fig. 10 a) and b) are strait lines parallel to E-axis, thus totally independent from the energy level and of increasing value for higher powerlevels. The parameters l_{1ch} and w_{PCM} follow a similar trend represented by straight lines of varying slope. It is easier to analyze the variation of these two parameters in terms of discharge time represented by the color map on each plot. Focusing on plots c) and d) of Fig. 10, towards the zone of slow discharge (bottom-right) the curves iso-l_{1ch} and iso-w_{PCM} shows a decreasing slope, the dependency on the P is stronger than the one on the E.

The opposite behavior appears in the fast discharge zone (top-left)

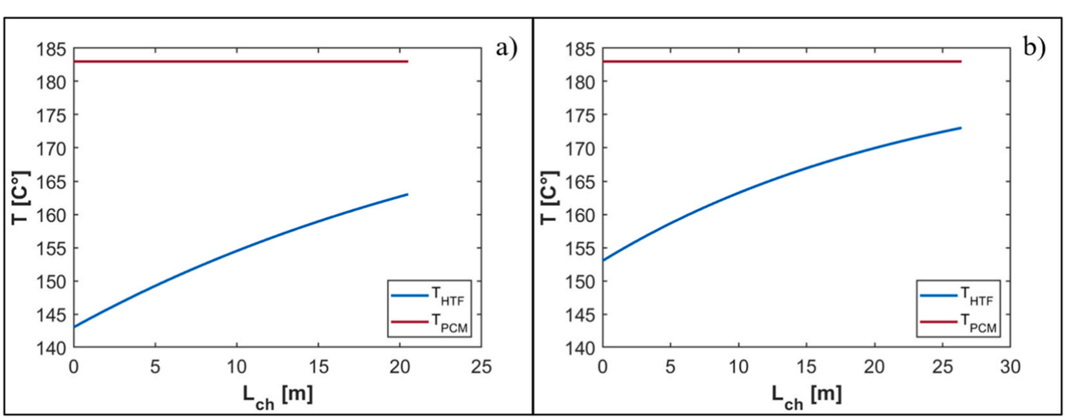

Fig. 9. Comparison of the evolution across the PP-LHTES: a) eutecticcompound PCM, P = 5 MW, E = 25MWh, $\Delta T_{\mathrm{pinch}} = 20$ °C, and b) eutectic compound PCM, P = 5 MW, E = 25MWh, $\Delta T_{\mathrm{pinch}} = 10$ °C.

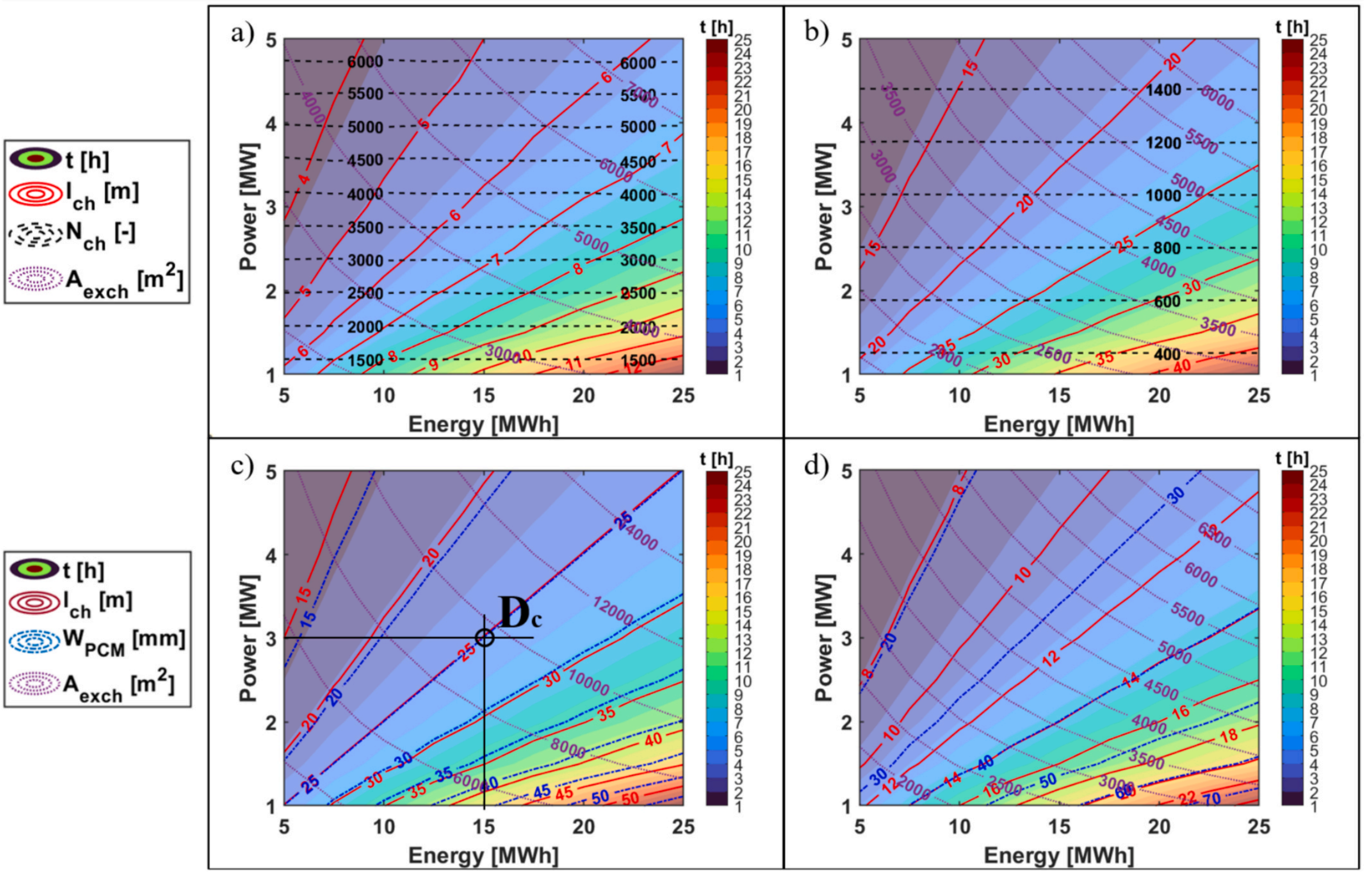

Fig. 10. Thermal design maps: a) eutecticcompound PCM, $\Delta T = 5°C$, T_{melt}=183 °C, b) eutecticcompound PCM, $\Delta T = 20$ °C, $T_{melt} = 183$ °C, c) organic PCM, $\Delta T = 10$ °C, T_{melt}=165 °C, $k_{PCM} = 0.19$ W/m/K, and d) eutectic compound PCM, $\Delta T = 10$ °C, T_{melt}=183 °C, k_{PCM}= 0.59 W/m/K.

where the curves have an increasing slope, meaning that they are more dependent on E than P. In both cases, the curves perfectly fall in a specific time range showing a very strong dependency on t_{disch}. Moreover, by comparing the plots two by two the effects of ΔT and k_{PCM} can be visualized. Plots a) and b) are refer to two different ΔT, the values of l_{1ch} are higher, N_{ch} are lower and A_{exch} are lower in the case of bigger ΔT comparing the same t_{disch} zones. Plots c) and d) consider two different PCM types with different k_{PCM}. When the parameter k_{PCM} is higher the systems present shorter channels and higher values of w_{PCM}, while for a lower value of k_{PCM} the channels are longer, and the pitch of plates is smaller. This analysis indicates that the optimal design varies based on discharge time and temperature difference. For systems requiring a slow discharge time and a large ΔT, the most effective configuration consists of a small number of long channels with a medium pitch between the pillow plates (PPs). In contrast, systems designed for fast discharge and a large ΔT feature a high number of short channels with a small pitch between the PPs. When both slow discharge and a small ΔT are required, the ideal setup includes a small number of long channels with a medium pitch between the PPs. Finally, for fast discharge and a small ΔT, the best configuration involves a high number of short channels with a large pitch between the PPs. For each case, the use of PCMs with high values of k_{PCM} would be beneficial to limit the size of the system by reducing A_{exch}.

4.2.1. *Performance comparison*

The performances evaluated with the design maps can be compared to those of different heat exchangers employed in LHTES. The study from Delgado-Diaz et al. [36] represents an interest starting point since it compare numerous types of heat exchange technologies applied to LHTES with similar PCM characteristics those considered in this paper,

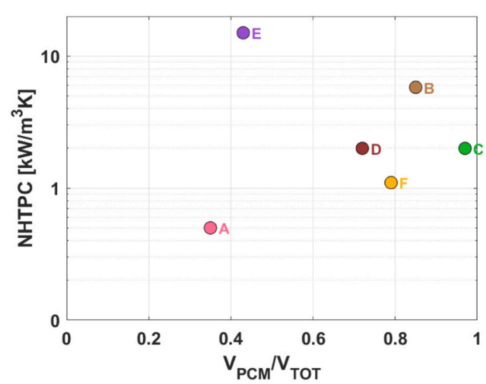

Fig. 11. Performance and compactness comparison between different HEX technologies applied to LHTES.

in particular T_{melt} in the range 4 °C to 305 °C. Delgado-Diaz et al. [36] compare the different technologies with a two-parameter graphics. The first parameter on the x-axis is the unit volume of PCM defined as V_{PCM}/V_{tot}, this parameter is suggested as an indicator of the energy density attainable by the system. The second parameter on the y-axis is the normalized heat transfer performance coefficient called NHTPC. This parameter is used to represent the heat transfer behavior regardless of the final dimensions, operation conditions, and overall scale and it is defined as $(UA)/V_{tot}$. The technologies investigated by Delgado-Diaz et al. [36] are reported in Fig. 11:

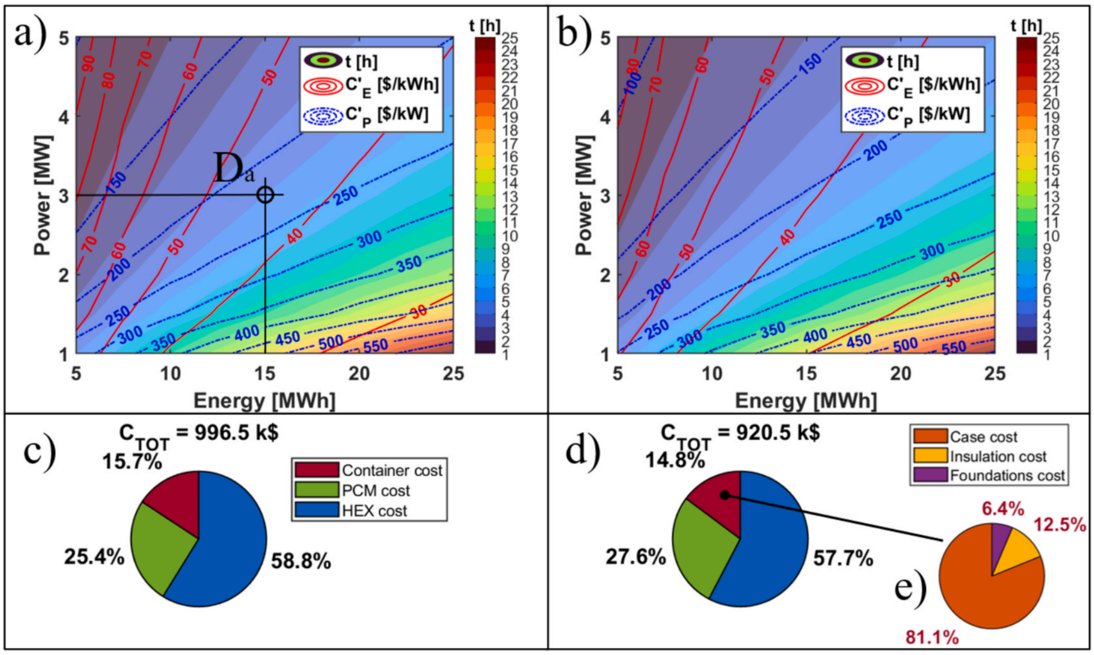

Fig. 12. Result of the economic assessment: a) cost map of the case: Eutectic compound PCM, $\Delta T = 5$°C, $_{melt}$=183 °C, b) cost map of the case: Eutectic compound PCM, $\Delta T = 20$ °C, T_{melt}=183 °C, c) pie chart of the main costs for E = 25MWh and P = 5 MW, d) Pie chart of the main costs for E = 25MWh and P = 5 MW, and e) Pie chart of the previous container costs.

A Macroencapsulated
B Carbon-based and Metal Foams
C Capillary Tube Bundle
D Tube and Finned Tube Bundle
E Automotive HEX

The value of the two parameters were evaluated for the PP technology and they are reported in Fig. 11 as the point F.

The PP technology performs well in terms of both compactness and thermal efficiency. Although it does not rank highest in this graph, its strength lies not only in its strong thermal performance and compact design but also in its lower production costs. A detailed cost comparison was not conducted in this study, as the primary objective is to demonstrate the potential of this methodology across various research areas.

4.3. Exploration of economic performance

The economic maps were built for the same P and E values as the design maps. Once the point of interest is found, as P = 3 MW, E = 15MWh, point "Da" in Fig. 12a, the values of the energy capacity cost (C'_E) and power capacity cost (C'_P) are obtained $\left(C'_{E,Da} = 45\$/KWh, C'_{P,Da} = 225\$/kW\right)$. The curves of C'_E have a parabolic trend in the range of values from 30 to 90 $/MWh. The zones of slow discharge present smaller values of C'_E concerning the fast discharge zone. The slope of the C'_E curves increases towards the fast-discharge zone, meaning the values of C'_E are strongly dependent on the P level in this region. The C'_P curves, show decreasing values towards the slow-discharge zone in the range between 100 and 550 $/kW in plots a) and b). In this zone (bottom-right), the parameter C'_P is strongly dependent on the power level as the slope of the curve reduces, thus, with a small variation of P the power cost undergoes a big variation.

Big systems with high values of E and high P represent the best compromise between optimal values of C'_E and C'_P.

In Fig. 12, plot (a) illustrates the cost map for systems designed with a small ΔT, while plot (b) presents the cost map for systems designed with a large ΔT. The PCM used in both cases remains the same to eliminate the impact of its thermal conductivity k_{PCM} on performance and to ensure that the cost assessment is not influenced by variations in PCM cost. The configuration designed for higher ΔT gives lower values of C'_E and C'_P. The higher ΔT configuration also brings a lower total cost, 7.6 % less than the small ΔT configuration, considering the biggest system (P = 5 MW, E = 25MWh) in both cases. The two pie charts reported in Fig. 12, highlights that C_{HEX} represent the biggest contribution to the total cost with a share of about 58 % while the container cost represents the smallest contribution. Fig. 12e) illustrates the contributions of C_c, C_{ins}, C_f to form C_{cont}. C_c is the biggest value due to the huge amount of SS needed for the case. A possible solution to reduce costs and reduce the amount of material used for the case could be to make use of light but highly resistant composite materials.

Table 5
REN heat production in real case studies from [37].

Industrial sector	Industry	REN [MWh/day]	Source
Chemicals	Plastics	1.343	[38]
Food	Brewery	1.372	[39]
Food	Dairy	1.589	[40]
Metals	Iron and steel	5.314	[41]
Wood and paper	Sawmill	0.375	[41]
Textile	–	5.110	[42]

4.4. Exemplary case study

The proposed methodology will now be applied to a realistic case study taken from literature and a PP-LHTES for industrial application will be designed. The study of Wolde et al. [37] suggests many study cases from literature in which the integration of TES was necessary in coupling with REN as heat sources for industrial processes, some of the proposed cases are reported in Table 5.

The study conducted by [39] serves as a valuable reference for integrating a PP-LHTES. It focuses on a medium-sized brewery in southern Scotland with an annual production of 250,000 hl. Brewing operations take place seven days a week for approximately 300 days per year. The process consists of several stages. Initially, malted barley is combined with hot water at 80 °C in the hot liquor tank. Following the mixing phase, the mixture undergoes an idle period, remaining at approximately 65 °C. The used grain is then separated and repurposed as animal feed for local farms. The remaining liquid is transferred to the copper vessel, where hops are added, and the mixture is boiled. After 4 % of the total liquid evaporates, the solution moves to the whirlpool, where hops and sediment are separated. Before fermentation begins, the liquid is cooled using a heat exchanger, reducing the temperature from 97 °C to 20 °C, while simultaneously heating the feed water from 8 °C to about 68 °C. The heated water is then pumped into the hot liquor tank and stored for later use.

The existing heat recovery system preheats the feed water during wort transfer from the whirlpool to the fermentation tanks. Heat is stored in both the bottom and top hot liquor tanks to enable indirect heat transfer to process water. However, no heat recovery is currently implemented for vapor from the copper vessel or flue gases from the boilers. The heating demand of the brewery is approximately 47.1 kWh per hectolitre.

Eiholzer et al. [39] assessed the impact of integrating solar collectors to partially meet the heat demand of the plant. In contrast, this study proposes a heat recovery system (HRS) incorporating a PP-LHTES. The analysis will begin with an assessment of the current system, followed by the application of the proposed methodology from input data acquisition to data processing, finishing with the final design of the PP-LHTES.

4.4.1. Input data acquisition

In the reference study, heat losses from the flue gases were analyzed, amounting to approximately 3.65 GWh per year at temperatures ranging from 101 °C to 170 °C. Given 300 operating days annually, this corresponds to a daily energy loss of about 12.16 MWh, representing a substantial amount of recoverable energy. This lost energy could be captured, stored in a PP-LHTES, and utilized as needed.

Assuming the lowest temperature of 101 °C, the recovered heat could be used to support the water heating process, raising its temperature from 68 °C to 80 °C before entering the THLT. The preheating phase lasts approximately 120 min and occurs every 240 min. This cycle indicates that a single PP-LHTES unit would be sufficient to meet the demand. The inlet temperature profile for this process is illustrated in Fig. 13, while Table 6 presents the input parameters obtained from the reference case.

The system will be designed to ensure that the discharge phase maintains a temperature increase from 68 °C to at least 80 °C throughout its duration. Consequently, the selected PCM must have a solidification temperature above 80 °C. Potassium aluminum sulfate (PAS) has a melting point of 105 °C, making it an ideal choice for this application. Considering a pinch temperature difference of approximately 10 °C to 15 °C between the PCM and the HTF, $KAl(SO_4)_2$ is identified as the most suitable PCM. Water has been chosen as the HTF based on the application requirements. Table 7 provides the thermal properties of potassium aluminum sulfate.

Table 6
Input properties applied in the model of the LHTES system.

Property	Value	Unit
t_{charge}	4	h
t_{disch}	2	h
$\dot{m}_{tot,disch}$	16.46	kg/s
$T_{in,disch}$	68	°C
$T_{out,disch}$	80	°C
$T_{in,charge}$	140	°C
$T_{out,charge}$	>100	°C
P_{disch}	0.83	MW
E_{tot}	1.7	MWh

Table 7
Properties of potassium aluminum sulfate from [43,44].

Property	Value	Unit
ρ_{PAS}	1550	$\frac{kg}{m^3}$
L_{PAS}	184	kJ/kg
$T_{melt.PAS}$	105	$^{\circ}C$
k_{PAS}	0.5	$\frac{W}{mK}$
cp_{PAS}	550	J/kgK

4.4.2. Application of the design model

The design model was configured with a discretization approach for energy and power values to generate more precise design and cost maps within a narrower range. Specifically, the power (P) levels range from 0.25 MW to 1.5 MW, with increments of 0.125 MW, while the energy (E) levels span from 0.5 MWh to 2 MWh, with increments of 0.25 MWh. The design process will focus on the discharge phase, as it demands the highest power output. The inputs for the design model are summed up in Table 8.

4.4.3. Design maps

The results obtained by the design model are the design and cost maps. The former is a map describing the trend of the main design parameters, which are N_{ch}, w_{PCM}, l_{ch} and A_{exch}. The design map is illustrated in Fig. 14. The shape remains similar to the maps presented in chapter 6.1.4, in fact, the iso-N_{ch} curves are parallel to the E axis, therefore considering the same P value, the value N_{ch} is totally independent from the E level. The iso-w_{PCM} curves as well as the iso-l_{ch} curves present constant values within the different time zones, meaning that considering the same discharge time the values w_{PCM} and l_{ch} are constant. Both w_{PCM} and l_{ch} increase their value for a longer discharging time. The curves iso-A_{exch} follow a hyperbolic trend, the values of A_{exch} increase for bigger P and E levels. Within Fig. 14 is highlighted as the working point during discharge calculated in the section "*Input data acquisition* ". Each

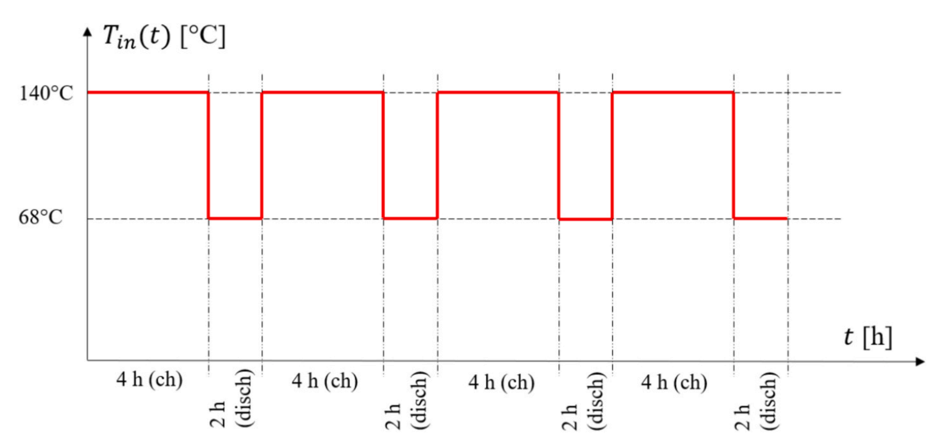

Fig. 13. Input curve of the inlet temperature for the PP-LHTES system.

Table 8
Input data for the design model of the case study.

Design input data	Value	Unit of measurement
E_{tot}^{targ}	0.5–2	MWh
t^{targ}	0.33–8	h
T_{in}	68	°C
T_{out}^{targ}	80	°C
PCM properties		
ρ_{PCM}	1550	kg/m3
k_{PCM}	0.5	W/m/K
cp_{PCM}	550	J/kg/K
L_{PCM}	184	kJ/kg
T_{melt}	105	°C
HTF properties		
ρ_{HTF}	994	kg/m3
k_{HTF}	0.626	W/m/K
cp_{HTF}	4068.5	J/kg/K
μ_{HTF}	$0.7006 \bullet 10^{-3}$	kg/m/s
Re	8000	–
Pillow plate input		
s_T	100	mm
$2s_L$	100	mm
w_{pp}	10	mm
k_{met}	15	W/m/K

working point is named Wp on the maps. This specific working point is drawn for E = 1.7 MWh and P = 0.83 MW, the values of the design parameters at the working point are reported in Table 9.

4.4.4. *Cost maps and economic impact*

Once the design parameters are determined, it is essential to establish the primary dimensions of the plates and, consequently, the overall system. Two key parameters to define are the number of turns within each plate and the number of channels forming a single plate, both of which significantly impact the cost maps. Typically, these parameters are constrained by the maximum allowable system size; however, in this case study, no such limitations are specified. As a result, three different design solutions will be explored::

A high number of channels per plate and low number of plates
B low number of channels per plate and high number of plates
C medium number of channels per plate and medium number of plates

Table 9
Main performance parameters computed for the case study.

Parameter	Value	Unit
E	1.7	MWh
P	0.83	MW
t	~ 2	h
N_{ch}	340	–
w_{PCM}	38	mm
l_{ch}	16.2	m
A_{exch}	1101	m^2

Table 10
Investigated number of channels and number of plates data.

Configuration name	Nch / plate	Npl	Ntrn
A	15	23	5
B	5	68	5
C	10	34	5

These three configurations will be investigated with the use of the cost maps, the one with the lower cost will be chosen. The data investigated for each configuration is reported in Table 10. For this evaluation, the cost of the PCM is taken from an important chemical supplier [45] while the cost of SS, insulation and foundation remains the same as the evaluation done in Section 4.

The costs were evaluated for each case for the design E and P levels (E = 1.7 MWh and P = 0.83 MW). The results are summed up in Table 11. The cheapest case resulted in case B with a low number of channels per plate, a high number of plates.

The cost map of case B is illustrated in Fig. 15, the map is drawn for P values in the range from 0.25 to 0.83 MW and E values in the range between 0.5 and 1.7 MWh.

The point in the in the top-right corner represents the design point of P = 0.83 MW and E = 1.7 MWh. The energy capacity cost for the design point is$C\prime_E$ ~ 160 \$/kWh, while the power capacity cost is$C\prime_P$ ~ 340 \$/MW. Given this map it would be possible to evaluate other design points to define the best solution for each objective, find the most economical solution or the most performant solution, but this overcomes the boundaries of interest of this study since the design point is imposed by the input of the problem.

The results obtained from the cost maps are used for the evaluation of the net present value and the calculation of the payback time of the investment. The net present is evaluated as in (17).

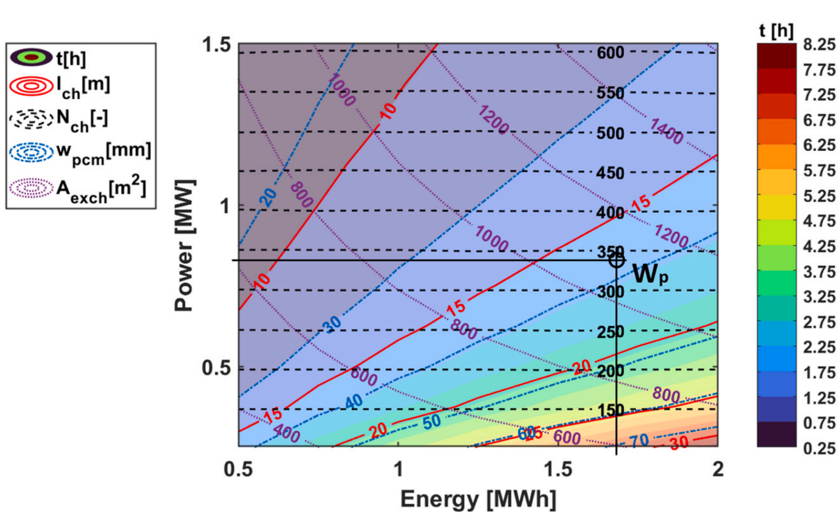

Fig. 14. Design map of energy, power and time obtained for the case study.

Table 11
Results of the economic evaluation carried out.

Parameter	A	B	C	Unit
C_{tot}	287.9	**268.7**	277.8	k$
C_{cont}	17.5	**11.6**	14.5	% of C_{TOT}
C_{PCM}	28.6	**30.7**	29.7	% of C_{TOT}
C_{HEX}	53.8	**57.7**	55.8	% of C_{TOT}
C_c	37.3	**59.3**	46.0	% of C_{cont}
C_{ins}	61.1	**32.9**	51.0	% of C_{cont}
C_f	1.6	**7.8**	3.0	% of C_{cont}
L_{tot}	2.7	**2.7**	2.7	m
H_{tot}	9	**3**	6	m
W_{tot}	0.253	**0.748**	0.374	m
N_{pl}	23	**68**	34	–

$$NPV = -C_{tot} + \frac{B_1}{(1-i)} + \frac{B_2}{(1-i)^2} + \ldots + \frac{B_n}{(1-i)^n} \tag{17}$$

Where $_n$ is the discount net cash flow considered evaluating the cost of natural gas saved with the introduction of the PP-LHTES subtracted by the cost of maintenance, calculated annually as 3 % of $_{tot}$. The cost of natural gas was found from UK natural gas cost statistics [https://ec.europa.eu/eurostat/statistics-explained/index.php?title=Natural_gas_price_statistics] considering the first semester of 2024. The coefficient i represents the weighted average cost of capital, in this case it has been calculated equal to 6.9 %. The payback time for this study case turned out to be 2.66 years, the evolution of net present value for a time span of 10 years is reported in Fig. 16a.

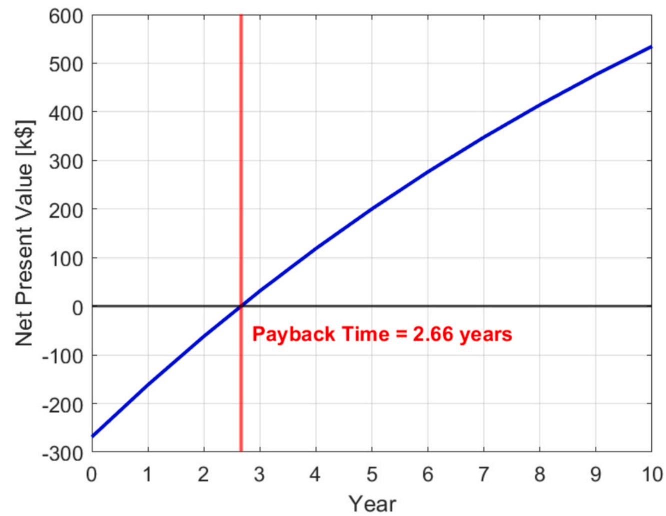

Fig. 16a. Evaluation of net present value for 10 years.

4.4.5. Dynamic model

The dynamic model is now set with the output data from the design model reported in Table 12.

The $T_{in}(t)$ curve is extrapolated from the reference as a cycle of 4 h charge at 140 °C and 2 h discharge at 68 °C, the curve is represented in Fig. 13. The value of the mass flow rate varies according to the charge and discharge phases, during charge, it is 8.5 kg/s while during discharge it is 16.46 kg/s. The behavior of the simulated system is illustrated in Fig. 16a and 16b. During discharge, the outlet temperature of the HTF never drops below 80 °C, as required by specifications. Additionally, the PP-LHTES reaches full charge at 140 °C after 4 h with a total mass flow rate of 8.5 kg/s, approximately half of the flow rate used during the charging phase. The designed PP-LHTES meets all constraints, confirming the validity of the design. The magnitude of the variation in temperature of the phase change material is lower than that of the heat transfer fluid during both phases. This is due to the lower thermal conductivity of the former substance.

Table 12
Input of the dynamic model.

Parameter	Value	Unit
A_{exch}	1101	m^3
$\dot{m}_{tot}$	8.5 –16.46	$\frac{kg}{s}$
s_T	100	mm
$2s_L$	100	mm
w_{pp}	10	mm
w_{PCM}	38	mm
$T_{in}(t)$	68 – 140	°C

4.4.6. Final design and considerations

The final design consists of a 3D representation of the designed system following the design parameters evaluated with the design model and deliberated with the dynamic model, these parameters and data are reported in Table 13. A 2D and 3D representation of the model can be visualized in Fig. 17 a) and b). In Fig. 17 a) are reported as the important dimensions of the system.

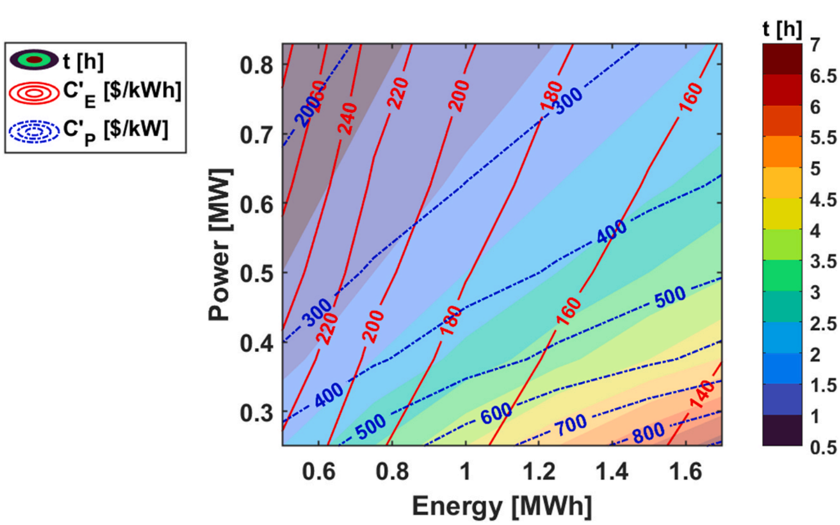

Fig. 15. Cost map determined for case B.

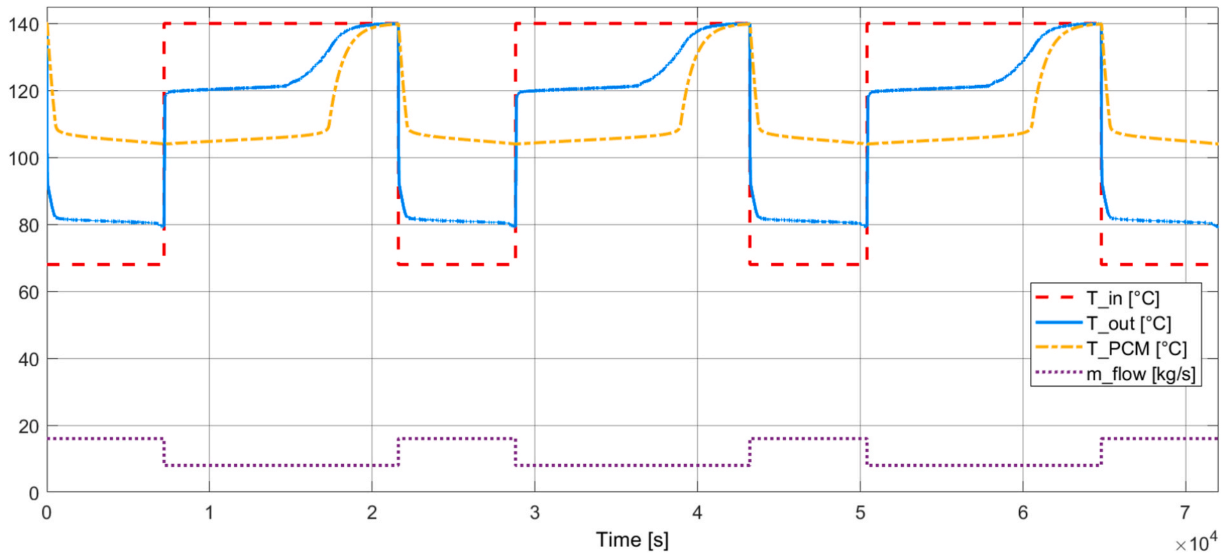

Fig. 16b. Dynamic behavior of the PP-LHTES for the case study.

Table 13
Final design parameters for the case study.

Parameter	Value	Unit
E	1.7	MWh
$P_{disch}(Re = 8000)$	0.83	MW
m_{PCM}	33,261	kg
N_{pp}	68	–
N_{ch}/pp	5	–
N_{trn}	5	–
w_{PCM}	38	mm
s_T	100	mm
$2s_L$	100	mm
δ_i	8	mm
w_{wall}	1	mm

This study aimed to demonstrate the application of the developed methodology to a real case study in which a PP-LHTES was integrated into a brewing plant to reduce both carbon emissions and operational costs. The input parameters were carefully assessed through an in-depth analysis of the reference case presented by [39]. The design model effectively determined the design parameters of the PP-LHTES based on these input values. Additionally, design maps were generated to provide a clear visual representation of how the energy-related parameters, E and P, influence the system design.

To identify the most cost-effective solution, three different system configurations with varying distributions of PP elements were analyzed. For each configuration, the total cost, the percentage contribution of each component cost like the PCM, containment, and heat exchanger, and the key system dimensions were evaluated. Since no strict spatial constraints were imposed on the system size, the most economical solution was selected.

Furthermore, the dynamic behavior of the system was assessed using a dynamic model to validate the design parameters and ensure optimal operational performance. This final evaluation phase was essential to confirm the capability of the system to meet the operational requirements of the reference case. The reliable methodology applied in this study successfully led to a PP-LHTES design that fully satisfies all predefined working constraints.

An integrated approach combining the steady-state and dynamic models presented in this study is recommended for the design of PP-LHTES systems. A further refinement of the proposed methodology would be its tuning with CFD and experimental data specifically derived for the peculiar study case considered. Modular design could also improve scalability and flexibility, allowing adaptation to various industrial applications.

5. Conclusions

Investing in sustainable solutions for energy efficiency and production is becoming increasingly important. The industrial sector, due to its

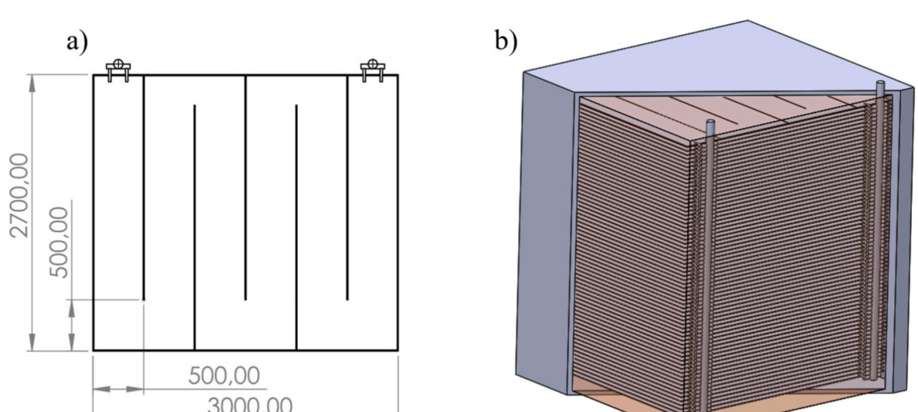

Fig. 17. Two-dimensional and three-dimensional representations of the PP-LHTES system for the case study.

high energy consumption, particularly for process heat, is a key area for decarbonization. This transition is only achievable through the integration of renewable energy sources, which, however, face challenges related to fluctuations in energy production. To mitigate or even eliminate this issue, renewable sources can be combined with energy storage solutions. Specifically, for process heat applications, thermal energy storage (TES) systems provide a viable solution.

This study focuses on latent heat thermal energy storage (LHTES) with a pillow-plate heat exchanger configuration. A thorough review of the available literature revealed a significant lack of data on this technology. The objective of this research was to expand the existing knowledge on PP-LHTES by evaluating its performance and economic feasibility through the development of an innovative methodology for both system design and dynamic simulation.

The proposed methodology consists of two main models: the design model and the dynamic model. The design model is an analytical, discretized approach used to determine the initial system parameters. It also generates design and cost maps, offering a clear understanding of how input parameters influence the final system configuration and cost. This model was validated against two comparative studies from the literature, demonstrating good accuracy with an error margin of approximately 10 %.

The dynamic model is an analytical tool capable of simulating the transient behavior of a PP-LHTES, using the equivalent heat capacity method to represent the phase change of the PCM. Validation against a reference study from the literature showed an error margin of approximately 2.8 %, confirming the reliability of the developed methodology.

The design model was used to investigate the design space of PP-LHTES and provide useful data to improve the understanding of this technology. A total of 27 configurations for possible industrial applications (E = 5–25 MWh, P = 1–5 MW) with different PCMs, T level and ΔT across the storage were analyzed and showed that the parameters w_{PCM} and l_{ch} strongly depends on the discharge time, N_{ch} is totally independent from the E value, considering the same P level, and A_{exch} is strongly dependent of both E and P level. Also, the economic aspect was investigated showing C'_E ranges between 30 and 90 \$/kWh while C'_P ranges between 100 and 550 \$/kW.

A final case study was carried out to demonstrate the application of the developed methodology under real operating conditions. A reference study from the literature provided a solid foundation for integrating a PP-LHTES into an industrial brewing plant. In this setup, a PP-LHTES powered by a heat recovery system replaced a gas boiler for preheating process water. The data obtained from the reference case served as input for the proposed methodology.

The design model was employed to determine the system parameters and identify the most cost-effective solution, while the dynamic model was used to simulate the transient behavior of the PP-LHTES based on the determined design parameters. The simulation results were positive, confirming that the designed storage system met all the performance requirements of the reference case.

This research represents a step forward in understanding the thermoeconomic potential of PP technology applied to LHTES. It not only introduces an innovative methodology for designing PP-LHTES but also systematically explores the design space and economic feasibility of this technology for industrial applications. Additionally, the study provides a practical case study to illustrate how the proposed methodology can be applied to a real-world design scenario.

CRediT authorship contribution statement

Giorgio Gioanola: Writing – original draft, Visualization, Validation, Software, Methodology, Investigation, Formal analysis, Data curation, Conceptualization. **Hector Bastida:** Writing – review & editing, Visualization, Supervision, Software, Methodology. **Elisa Guelpa:** Writing – review & editing, Validation, Supervision, Project administration, Investigation, Conceptualization. **Vittorio Verda:** Writing – review & editing, Validation, Supervision, Project administration, Investigation, Conceptualization. **Adriano Sciacovelli:** Writing – review & editing, Writing – original draft, Validation, Supervision, Resources, Project administration, Methodology, Investigation, Funding acquisition, Conceptualization.

Declaration of competing interest

The authors declare that they have no known competing financial interests or personal relationships that could have appeared to influence the work reported in this paper.

Acknowledgements

This work was supported by the Horizon Europe research and innovation program of the European Union (THUMBS UP Project with grant number 101096921; ZHENIT Project with grant number 101056801). Dr Adriano Sciacovelli acknowledges also UK Research and Innovation (UKRI) for financial support (Project Reference 10064507, 10038861).Authors would like to thank Dr Lorenzo Ciappi (University of Birmingham) for support and help in revision of the manuscript, verification of results and enhancement of figures.

Data availability

Data will be made available on request.

References

[1] I. Energy Agency, "Net Zero by 2050 - A Roadmap for the Global Energy Sector," 2050, Accessed: Feb. 20, 2025. [Online]. Available: www.iea.org/t&c/.
[2] Henry A, Prasher R, Majumdar A. Five thermal energy grand challenges for decarbonization. Nat Energy 2020;5(9):635–7. https://doi.org/10.1038/s41560-020-0675-9.
[3] Thiel GP, Stark AK. To decarbonize industry, we must decarbonize heat. Joule 2021;5(3):531–50. https://doi.org/10.1016/J.JOULE.2020.12.007.
[4] Rehfeldt M, Fleiter T, Toro F. A bottom-up estimation of the heating and cooling demand in European industry. Energy Effic 2018;11(5):1057–82. https://doi.org/10.1007/S12053-017-9571-Y/METRICS.
[5] Marina A, Spoelstra S, Zondag HA, Wemmers AK. An estimation of the European industrial heat pump market potential. Renew Sustain Energy Rev 2021;139:110545. https://doi.org/10.1016/J.RSER.2020.110545.
[6] Beccali M, Bonomolo M, Martorana F, Catrini P, Buscemi A. Electrical hybrid heat pumps assisted by natural gas boilers: a review. Appl Energy 2022;322:119466. https://doi.org/10.1016/J.APENERGY.2022.119466.
[7] Su Z, et al. Opportunities and strategies for multigrade waste heat utilization in various industries: a recent review. Energy Convers Manag 2021;229:113769. https://doi.org/10.1016/J.ENCONMAN.2020.113769.
[8] Wei M, McMillan CA, de la Rue du Can S. Electrification of industry: potential, challenges and outlook. Current Sustain/Renew Energy Rep 2019;6(4):140–8. https://doi.org/10.1007/S40518-019-00136-1/TABLES/1.
[9] Sharshir SW, et al. Thermal energy storage using phase change materials in building applications: a review of the recent development. Energ Build 2023;285:112908. https://doi.org/10.1016/J.ENBUILD.2023.112908.
[10] Steinmann WD. Thermal energy storage for medium and high temperatures: concepts and applications. Therm Energy Storage Medium High Temp: Concepts Applic 2021:1–395. https://doi.org/10.1007/978-3-658-02004-0/COVER.
[11] L. Ciappi, P. Niknam, R. Fisher, and A. Sciacovelli, "Application of flat plate latent heat thermal energy storage for waste heat recovery and energy flexibility in maritime sector," 36th International Conference on Efficiency, Cost, Optimization, Simulation and Environmental Impact of Energy Systems, ECOS 2023, pp. 2342–2353, 2023, doi: 10.52202/069564-0211.
[12] Ye WB, Arıcı M. Redefined interface error, 2D verification and validation for pure solid-gallium phase change modeling by enthalpy-porosity methodology. Int Commun Heat Mass Transfer 2023;147:106952. https://doi.org/10.1016/J.ICHEATMASSTRANSFER.2023.106952.
[13] Ye WB, Arıcı M. 3D validation, 2D feasibility, corrected and developed correlations for pure solid-gallium phase change modeling by enthalpy-porosity methodology. Int Commun Heat Mass Transfer 2023;144:106780. https://doi.org/10.1016/J.ICHEATMASSTRANSFER.2023.106780.
[14] Ye WB, Arıcı M. False diffusion, asymmetrical interface, and equilibrious state for pure solid-gallium phase change modeling by enthalpy-porosity methodology. Int Commun Heat Mass Transfer 2023;144:106746. https://doi.org/10.1016/J.ICHEATMASSTRANSFER.2023.106746.
[15] Ye WB, Arıcı M. Numerical thermal control design for applicability to a large-scale high-capacity lithium-ion energy storage system subjected to forced cooling.

Numeri Heat Transf A Appl 2024. https://doi.org/10.1080/10407782.2024.2344068.
[16] Vogel J, Keller M, Johnson M. Numerical modeling of large-scale finned tube latent thermal energy storage systems. J Energy Storage Jun. 2020;29:101389. https://doi.org/10.1016/J.EST.2020.101389.
[17] Pizzolato A, Sharma A, Maute K, Sciacovelli A, Verda V. Multi-scale topology optimization of multi-material structures with controllable geometric complexity — applications to heat transfer problems. Comput Methods Appl Mech Eng 2019;357:112552. https://doi.org/10.1016/J.CMA.2019.07.021.
[18] Laasri IA, Elmaazouzi Z, Outzourhit A, Mghazli MO. Investigation of different topology-optimized fin structures in a cylindrical latent heat thermal energy storage unit. Therm Sci Eng Prog 2022;33:101372. https://doi.org/10.1016/J.TSEP.2022.101372.
[19] Vogel J, Johnson M. Natural convection during melting in vertical finned tube latent thermal energy storage systems. Appl Energy 2019;246:38–52. https://doi.org/10.1016/J.APENERGY.2019.04.011.
[20] Ge R, Humbert G, Martinez R, Attallah MM, Sciacovelli A. Additive manufacturing of a topology-optimised multi-tube energy storage device: experimental tests and numerical analysis. Appl Therm Eng 2020;180:115878. https://doi.org/10.1016/J.APPLTHERMALENG.2020.115878.
[21] Mastani Joybari M, Selvnes H, Sevault A, Hafner A. Potentials and challenges for pillow-plate heat exchangers: state-of-the-art review. Appl Therm Eng 2022;214. https://doi.org/10.1016/J.APPLTHERMALENG.2022.118739.
[22] Piper M, Olenberg A, Tran JM, Kenig EY. Determination of the geometric design parameters of pillow-plate heat exchangers. Appl Therm Eng 2015;91:1168–75. https://doi.org/10.1016/J.APPLTHERMALENG.2015.08.097.
[23] Piper M, Zibart A, Tran JM, Kenig EY. Numerical investigation of turbulent forced convection heat transfer in pillow plates. Int J Heat Mass Transf 2016;94:516–27. https://doi.org/10.1016/J.IJHEATMASSTRANSFER.2015.11.014.
[24] Piper M, Zibart A, Kenig EY. New design equations for turbulent forced convection heat transfer and pressure loss in pillow-plate channels. Int J Therm Sci 2017;120:459–68. https://doi.org/10.1016/J.IJTHERMALSCI.2017.06.012.
[25] Lin W, Zhang W, Ling Z, Fang X, Zhang Z. Experimental study of the thermal performance of a novel plate type heat exchanger with phase change material. Appl Therm Eng 2020;178:115630. https://doi.org/10.1016/J.APPLTHERMALENG.2020.115630.
[26] O. Galteland, M. Gouis, J. Salgado-Beceiro, and A. Sevault, "Fourteen months operation of a 200 kWh latent heat storage pilot," *2023 8th International Conference on Smart and Sustainable Technologies, SpliTech 2023*, 2023, doi: 10.23919/SPLITECH58164.2023.10193589.
[27] Niknam PH, Ciappi L, Sciacovelli A. Latent heat thermal energy storage system with pillow-plate heat exchangers topology – assessment of thermo-fluid dynamic performance and application potential. Appl Therm Eng 2025;265:125606. https://doi.org/10.1016/J.APPLTHERMALENG.2025.125606.
[28] Nithyanandam K, Pitchumani R. Cost and performance analysis of concentrating solar power systems with integrated latent thermal energy storage. Energy 2014;64:793–810. https://doi.org/10.1016/J.ENERGY.2013.10.095.
[29] Pereira da Cunha J, Eames P. Thermal energy storage for low and medium temperature applications using phase change materials – a review. Appl Energy 2016;177:227–38. https://doi.org/10.1016/J.APENERGY.2016.05.097.
[30] "Plate Heat Exchanger Cost Estimation," *Low Grade Heat Driven Multi-Effect Distillation and Desalination*, p. 173, 2017, doi: 10.1016/B978-0-12-805124-5.15005-3.
[31] "Global Steel Prices, Indexes & Forecasts | MEPS International." Accessed: Feb. 21, 2025. [Online]. Available: https://mepsinternational.com/gb/en.
[32] B. Kelly and D. Kearney, "Thermal Storage Commercial Plant Design Study for a 2-Tank Indirect Molten Salt System: Final Report; May 13, 2002 - December 31, 2004," 2002, Accessed: Feb. 21, 2025. [Online]. Available: http://www.osti.gov/bridge.
[33] Sevault A, Vullum-Bruer F, Tranås OL. Active PCM-based thermal energy storage in buildings. Encyclopedia Energy Storage 2022;1–4:453–69. https://doi.org/10.1016/B978-0-12-819723-3.00008-1.
[34] "CrodaTherm 37 | Croda Industrial Specialties." Accessed: Feb. 21, 2025. [Online]. Available: https://www.crodaindustrialspecialties.com/en-gb/resources/resource-finder/resource/22500-crodatherm-37.
[35] Bastida H, De la Cruz-Loredo I, Ugalde-Loo CE. Effective one-dimensional dynamic modelling of latent heat thermal energy storage units for heating applications. IET Energy Syst Integr 2024;6(3):297–315. https://doi.org/10.1049/ESI2.12128.
[36] Delgado-Diaz W, Stamatiou A, Maranda S, Waser R, Worlitschek J. Comparison of heat transfer enhancement techniques in latent heat storage. Appl Sci 2020;10(16):5519. https://doi.org/10.3390/APP10165519.
[37] Wolde I, Cardemil JM, Escobar R. Compatibility assessment of thermal energy storage integration into industrial heat supply and recovery systems. J Clean Prod 2024;440:140932. https://doi.org/10.1016/J.JCLEPRO.2024.140932.
[38] Pag F, Jesper M, Kusyy O, Vajen K, Jordan U. Solar fractions of SHIP plants considering the availability of roof area based on OpenStreetMap data. Sol EnergyAdv 2022;2:100017. https://doi.org/10.1016/J.SEJA.2022.100017.
[39] Eiholzer T, Olsen D, Hoffmann S, Sturm B, Wellig B. Integration of a solar thermal system in a medium-sized brewery using pinch analysis: methodology and case study. Appl Therm Eng 2017;113:1558–68. https://doi.org/10.1016/J.APPLTHERMALENG.2016.09.124.
[40] Platzer WJ. Total performance assessment method for industrial process heat systems. Proceedings - ISES Solar World Congress 2021;2021:23–31. https://doi.org/10.18086/SWC.2021.01.04.
[41] K. Lovegrove *et al.*, "Renewable Energy Options for Industrial Process Heat - Australian Renewable Energy Agency (ARENA)." Accessed: Feb. 21, 2025. [Online]. Available: https://arena.gov.au/knowledge-bank/renewable-energy-options-for-industrial-process-heat/.
[42] Frein A, Calderoni M, Motta M. Solar thermal plant integration into an industrial process. Energy Procedia 2014;48:1152–63. https://doi.org/10.1016/J.EGYPRO.2014.02.130.
[43] Jayathunga DS, Karunathilake HP, Narayana M, Witharana S. Phase change material (PCM) candidates for latent heat thermal energy storage (LHTES) in concentrated solar power (CSP) based thermal applications - a review. Renew Sustain Energy Rev 2024;189:113904. https://doi.org/10.1016/J.RSER.2023.113904.
[44] Lee KS, Lee CE. Molar heat capacity of potassium alum KAl(SO4)2 ·12H2O at low temperatures: revisited with determination of the debye temperature. J Korean Phys Soc 2018;72(3):379–83. https://doi.org/10.3938/JKPS.72.379/METRICS.
[45] Lerochem, "Potassium Aluminium Sulfate (Potassium Alum), kg Product size, kg 1 kg." Accessed: Feb. 21, 2025. [Online]. Available: https://lerochem.eu/en/pagrindinis/90-447-potassium-aluminium-sulfate-potassium-alum-kg.html?srsltid=AfmBOoqPTS8A_PqLjWbY77BnlmJ3voNPwH6rsultYR-eDrusE2GvJTWL.